Combined experimental and theoretical study of thin hafnia films

X. Luo,[1] A. A. Demkov,[1,*] D. Triyoso,[2] P. Fejes,[3] R Gregory,[3] and S. Zollner[4]
[1]*Department of Physics, The University of Texas at Austin, Austin, Texas 78712, USA*
[2]*Freescale Semiconductor, Inc., Austin, Texas 78721, USA*
[3]*Freescale Semiconductor, Inc., Tempe, Arizona 85284, USA*
[4]*Freescale Semiconductor, Inc., Hopewell Junction, New York 12533, USA*
(Received 29 July 2008; revised manuscript received 3 November 2008; published 12 December 2008)

We present a joint experimental and theoretical study of ultrathin hafnia films grown on Si (001) by atomic layer deposition for applications as a gate dielectric of a field-effect transistor. The structural analysis by means of high-resolution transmission electron microscopy, electron diffraction, and x-ray diffractometry indicates films with thickness of 4 nm or less to be polycrystalline, predominantly monoclinic and textured, with the texture axis being the normal to the $(21\bar{1})$, $(11\bar{2})$, and their equivalent planes. Films with thickness around 10 nm consist of a mixture of monoclinic and tetragonal phases more or less randomly oriented. Films thicker than 25 nm are purely monoclinic with $(\bar{1}11)$ and (111) textures. Using density-functional theory we investigate surface energies of monoclinic and tetragonal hafnia films in search for thermodynamic means of controlling the film microstructure. We report the atomic and electronic structures of these films including the surface energy, work function, and electron affinity.

DOI: 10.1103/PhysRevB.78.245314 PACS number(s): 73.20.−r, 73.30.+y

I. INTRODUCTION

Hafnia-based dielectric films have replaced silica as a gate dielectric in the current generation of field-effect transistors (FETs).[1,2] Hafnia is used due to its thermodynamic stability against Si,[3,4] wide band gap, and high dielectric constant (k =20–25).[5] The high dielectric constant (or high k) of hafnia allows maintaining the gate capacitance and therefore the drain-source saturation current without reducing the oxide thickness. Thus the use of high-k dielectrics enables continuous scaling of the complimentary metal oxide semiconductor (CMOS) technology known as Moore's law. There are a variety of methods of hafnia film deposition on different substrates, including atomic layer deposition (ALD),[6] pulse laser deposition (PLD),[7] and chemical vapor deposition (CVD).[8] Thin hafnia films are typically amorphous as deposited and polycrystalline after a postdeposition annealing; some are mixed phase and textured. Hafnia films deposited at 300 °C by ALD are reported to be polycrystalline, mixed phased, predominantly monoclinic with $(\bar{1}11)$ texture.[9,10] Other studies report hafnia films consisting of predominantly monoclinic grains preferring (001) and (111) growth directions.[11] The structure-property relation of thin hafnia films is not completely clear. Because different phases, orientations, and terminations of surfaces may lead to nonuniformity in the electrical properties of the film, a deeper understanding of the microscopic nature of these films is critically important to the further scaling of the CMOS technology.

The difficulty in controlling the structure and properties of hafnia films is rooted in the complexity of transition-metal oxides such as HfO_2. In recent years the bulk properties of hafnia, such as structure, electronic spectrum, and dielectric constant, have been studied theoretically.[5] However, thin hafnia films behave differently from bulk hafnia, in particular, phase transitions occur at much lower temperature.[7] In addition, the properties of hafnia surface may play a role in the gate dielectric film due to its high surface area to volume ratio. In this paper we report a joint experimental and theoretical study of hafnia films of different thicknesses deposited by ALD and characterized by transmission electron microscopy (TEM), electron diffraction (ED), x-ray diffractometry (XRD), and density-functional theory (DFT) to provide more insights into hafnia films. In particular, using first-principles calculations we study theoretically the hafnia surface. Previous theoretical studies of hafnia surface[12,13] are limited to stoichiometric surfaces of the monoclinic phase. However, experiment indicates that hafnia films are polycrystalline with more than one phase present.[6–8] Thus a systematic study of hafnia surface including monoclinic and tetragonal phases for both stoichiometric and nonstoichiometric terminations is of interest. The rest of the paper is organized as follows. In Sec. II we describe the atomic layer deposition of thin hafnia films. The structural characterizations by means of high-resolution transmission electron microscopy (HRTEM) and XRD are reported in Sec. III. In Sec. IV we present a systematic theoretical study of surfaces of monoclinic and tetragonal hafnia.

II. ATOMIC LAYER DEPOSITION OF THIN FILMS OF HAFNIA

Among many explored deposition techniques for gate dielectrics, atomic layer deposition[2,10,14] poses many advantages such as excellent thickness control, conformality, and low-temperature deposition.[15] The first study on ALD HfO_2 for gate dielectric applications was performed on films deposited using hafnium tetrachloride $HfCl_4$ and water H_2O.[16] Since then, many reports on film growth and properties of $HfCl_4$-based HfO_2 have been published.[10,14,17,18] Excellent metal oxide semiconductor field-effect transistor (MOSFET) characteristics have been reported.[19] $HfCl_4$ has advantages of (1) being carbon free, (2) being relatively small in size (less steric hindrance), (3) being inexpensive, and (4) having a wide ALD window (up to 750 °C).

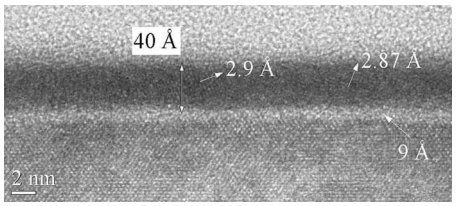

FIG. 1. Cross-section TEM image of the 40 Å HfO_2 film. The film thickness, measured from this image, is 40 Å with a 9 Å interface layer between the HfO_2 film and the substrate. Measurements of a few lattice fringe spacings in the HfO_2 are indicated on this image (the arrow, in each case, is normal to the lattice fringes).

In this study, the HfO_2 films are formed via ALD using hafnium tetrachloride and water at 300 °C as reported previously.[10,14] The HfO_2 film thickness is controlled by the number of cycles deposited. One deposition cycle consists of a water pulse, a nitrogen purge (to remove unreacted water), a $HfCl_4$ pulse, and a nitrogen purge. As received silicon wafers are cleaned using a solution of de-ionized water, hydrogen peroxide, and hydrochloric acid with a ratio of 40:2:1 at 35 °C for 10 min. This so-called "SC2 clean" grows a thin chemical oxide layer on the silicon substrate. HfO_2 is deposited on chemical oxide starting surfaces. After deposition, hafnia films are either not annealed at all or annealed in oxygen for 60 s at 500 °C.

III. STRUCTURAL ANALYSIS

A. Transmission electron microscopy

Electron-diffraction analysis is done on thin HfO_2 films (<200 Å thick) deposited by ALD at 300 °C and subject to a postdeposition annealing at 500 °C for 60 s. The hafnia and interfacial layer thicknesses are determined by cross-section TEM. A Philips CM200 FEG TEM operating at an accelerating potential of 200 kV is used for the imaging and electron diffraction.

A cross-section image of the thinnest film studied is shown in Fig. 1. The HfO_2 film is 40 Å in thickness with a 9 Å interface layer. The crystalline nature of the film can be seen from the lattice fringes visible in the film. A few lattice spacings could be measured in the film (indicated on the image) but not sufficient to determine either a crystallographic structure or possible texturing. In order to characterize the crystalline structure of the films, diffraction patterns from plan-view TEM samples are analyzed.

To prepare the plan-view samples, the substrate silicon is removed from the back side of the wafer by mechanical polishing, with a final thinning done using an Ar ion mill. In most areas of the sample, some thin Si is still covering the HfO_2 film. The silicon diffraction spots from these areas are used to calibrate the camera length for the HfO_2 diffraction analysis. Diffraction patterns are taken with the beam at normal incidence to the plane of the HfO_2 film and also with the sample tilted by 40° from this orientation to give information about texturing of the hafnia grains. For all of the films down to 73 Å in thickness, the diffraction pattern does not change on tilting of the sample, indicating a lack of texturing of the hafnia grains. For the 40 Å film, however, the continuous diffraction rings broke up into arcs, indicating texturing in this film as seen in Fig. 2.

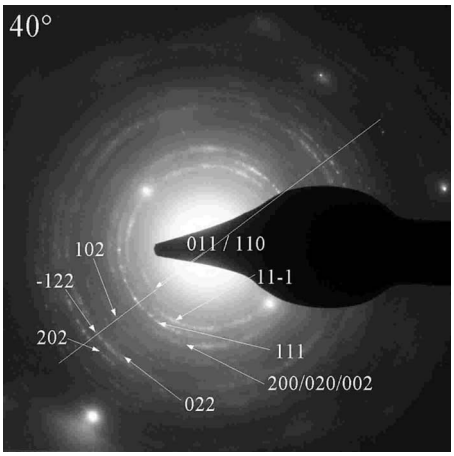

FIG. 2. Electron-diffraction pattern from the 40-Å-thick hafnia film with the film tilted 40° to the incident electron beam. The presence of arcs after tilting the film, rather than continuous rings, is an indication of the texturing in this film.

To determine both the crystalline structure and texturing present in the films, line profiles are taken in a radial direction from the centers of the patterns. The diffraction patterns used for this analysis are those taken with the incident beam normal to the plane of the HfO_2 films. The camera length is carefully calibrated using the silicon diffraction spots, and the radii of the various diffraction rings are determined by multiple-peak fitting to the line profiles. Figure 3 shows the fitted diffraction peaks superimposed on a section of the diffraction pattern line profiles for both the 99 and 40 Å hafnia films. All of the thicker films have diffraction patterns similar to the 99 Å film shown here. It is only the 40 Å film that shows any variation from the thicker films.

The monoclinic phase of hafnia is present in both films, though some of the diffraction peaks are missing, or at least weak, in the 40 Å film because of texturing in this film. The thicker films all contain a second phase which gives a strong diffraction peak corresponding to a d spacing of 2.94 Å. The structure of this second phase is not totally clear but we assign it to the tetragonal phase for the following reason.

The expected positions of the strongest diffraction peaks, calculated from the lattice parameters given in the JCPDF powder-diffraction database,[20,21] are indicated in Fig. 3 for both the cubic and tetragonal phases. The position of the peak from the second phase lies much closer to the cubic 111 peak (lattice spacing=2.94 Å) than for the tetragonal 111 peak (lattice spacing=2.99 Å). This tetragonal 111 peak is not indexed, even though it is listed as a strong peak in the powder-diffraction database[20] because it is forbidden in the space group assigned to the structure (space-group No. 137: $P4_2/nmc$). This space group is likely not correct for two reasons. It does not agree with the given diffraction data and the tetragonal HfO_2 structure is expected to be similar to the ZrO_2 structure, which has a space group of $P\bar{4}m2$ (space-group No. 115). Assigning this space group to the structure is consistent with the given diffraction data, and in particular,

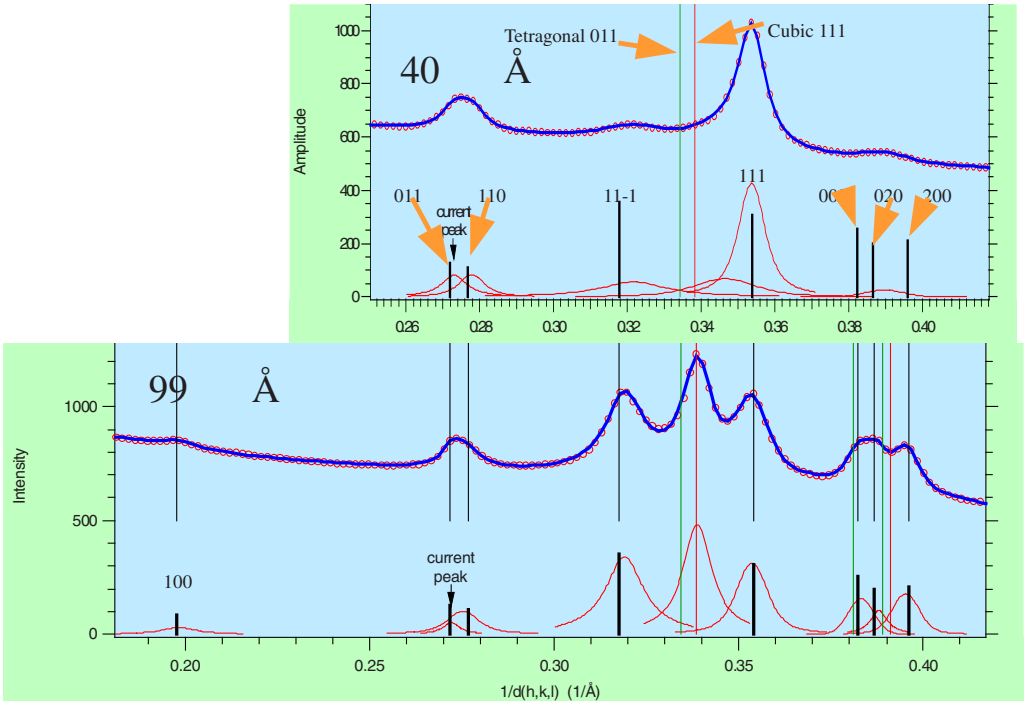

FIG. 3. (Color online) Electron-diffraction pattern line profiles for two HfO_2 films (40 and 99 Å thick). The red dots represent the measured line profiles. The blue curve superimposed on the data is the fitted profile using a multiple-peak fitting routine. The individual red curves are the individual peaks that were fitted to the data. Vertical solid black lines at the bottom of the chart represent the positions of the diffraction peaks calculated from the monoclinic HfO_2 structure. The heights of these lines are proportional to the calculated intensities for each diffraction peak. The vertical red lines represent the positions of the diffraction peaks from the cubic HfO_2 structure, and the green lines represent the expected positions from the tetragonal HfO_2 structure.

the strongest reflection, 111, is no longer forbidden. The powder-diffraction database does not indicate the temperature at which the lattice parameters were measured, but similar values for the lattice parameters, reported in Ref. 22, are measured at temperatures above 1700 °C. At room temperature, the lattice parameters will be smaller, causing the diffraction peak to shift to a higher value of $1/d$. We could not find published values of the room-temperature lattice parameters for the tetragonal phase, but considering this shift to a higher d spacing, assigning the tetragonal 111 diffraction peak to the second phase seen in Fig. 3, is more reasonable than the cubic 111 peak.

The tetragonal structure is a high-temperature structure, normally existing only above 1700 °C, and which cannot be quenched to room temperature.[7] The tetragonal phase can exist at room temperature only below a critical grain size, which is reported to be between 40 and 100 Å under strain-free conditions.[7] Since in the films as thin as those being studied there are expected to be grains sufficiently small to sustain the tetragonal phase at room temperature, it is not unreasonable for some tetragonal phase to coexist with the monoclinic phase. The cubic structure is an even higher-temperature phase (>2800 °C) and so is even less likely to be seen at room temperature. We have therefore assigned the tetragonal phase as the second phase in these films.

By an analysis of the missing diffraction peaks in the 40 Å film, we can determine that the only possible low indexed texture axes normal to the film are the $\{21\bar{1}\}$ and $\{11\bar{2}\}$ crystal axes. The presence of grains with a {1,2,1} texture axis could not be ruled out, although this grain orientation would not contribute to the observed intensity in the 011 and 110 diffraction peaks. The other orientations that cannot be ruled out are the $\{\bar{1}11\}$ and {1,1,1} axes reported in Refs. 9–11. These, however, do not contribute to the 111 diffraction intensity which is the strongest observed diffraction peak, so these orientations cannot be a major constituent of the film.

B. X-ray diffraction

XRD is used to identify phases and characterize texture of HfO_2 films deposited to thicknesses of 200–230 Å. Scan data are acquired with coupled in-plane θ-2θ geometry (powder mode) using Cu $K\alpha$ radiation from a rotating anode (50 kV and 180 mA). The x-ray beam is conditioned with a 1° divergence slit (producing a planar wave) and a diffracted beam monochromator. Scan rate is 0.1°/s, and step size is 0.05°. Scans are taken with the sample tilted slightly off axis to dissatisfy the Bragg condition for the single-crystal substrate, thus reducing background counts from the substrate. Data are analyzed principally by reference to powder-diffraction files for tetragonal and monoclinic HfO_2. These are in the ICDD database.

Samples analyzed by XRD include one as deposited and two subjected to postdeposition annealings at 900 or 1000 °C for 60 s in flowing N_2. Figure 4 shows scan data for as-deposited and 900 °C-annealed films, overlaid together on the same plot. Both as-deposited and annealed films are

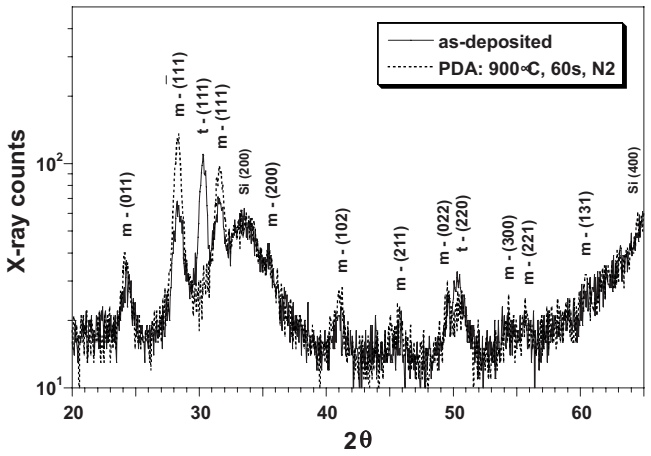

FIG. 4. XRD analysis for as-deposited thick HfO_2, showing a mixture of orthorhombic and monoclinic phases, and 900 °C post-deposition annealed HfO_2 showing only monoclinic phase material.

polycrystalline material. The as-deposited film has mixed monoclinic and tetragonal phases. The annealed film appears entirely monoclinic with $(\bar{1}11)$ and (111) textures. Line assignments are made with reference to powder-diffraction files (monoclinic HfO_2) (Ref. 21) and (tetragonal HfO_2).[20] The (111) line at 30° 2θ probably indicates tetragonal phase if one assigns the space-group $P\text{-}4m2$ (space-group No. 115) to this structure. XRD analysis for the HfO_2 film annealed at 1000 °C for 60 s revealed almost no difference in phase and texture compared to the 900 °C-annealed film.

C. Structure

Thicker HfO_2 films are analyzed by x-ray diffraction. After annealing at 900–1000 °C, these are determined to consist of the monoclinic phase with {1,1,1} and $\{\bar{1}11\}$ texturing. Films that are thinner than 200 Å do not provide good x-ray diffraction data, and so these are analyzed using electron diffraction. Films with thicknesses between 70 and 100 Å show no texturing after a 500 °C annealing and are found to consist of a mixture of monoclinic and tetragonal phases. The thinner 40 Å film, after the same annealing, shows only the monoclinic phase, which is textured along the $\{21\bar{1}\}$ and $\{11\bar{2}\}$ axes.

IV. THEORETICAL ANALYSIS

DFT calculations are carried out using the Vienna *ab initio* simulation package (VASP).[23] We use the PW91 generalized gradient approximation (GGA).[24,25] Vanderbilt-type ultrasoft pseudopotentials are employed.[26] For Hf atoms $5d$ and $6s$ electrons are included; for oxygen atoms $2s$ and $2p$ electrons are included. The Brillouin-zone integration is performed with a Monkhorst-Pack method. The kinetic-energy cutoff of 800 eV is found to be sufficient (the total energy is converged to 10^{-6} eV/cell and forces are converged to 10^{-3} eV/Å). For bulk calculations we use a relatively coarse $4\times4\times4$ grid size for the initial relaxation of the structure, which is followed by an accurate calculation with an $8\times8\times8$ grid to determine the final structure. For the surface calculations discussed below we use the $4\times4\times1$ and $8\times8\times1$ grids. Table I shows the structural parameters for three fully relaxed HfO_2 polymorphs; all are in good agreement with our and published data[28,29] and with previous calculations.[5,27] Our total-energy calculations reproduce the correct energetic ordering of hafnia phases: cubic to tetragonal to monoclinic going from the highest to the lowest energy phase.

TABLE I. The crystal structure parameters for the three relaxed HfO_2 polymorphs.

	Present GGA	Previous LDA[a]	Expt.[b]
		Cubic	
V (Å^3)	32.774	32.0	32.77
a (Å)	5.08	5.04	5.08
		Tetragonal	
V (Å^3)	33.28	32.5	
a (Å)	3.58	3.56	
c (Å)	5.19	5.11	
d_z (Å)	0.043	0.042	
		Monoclinic	
V (Å^3)	34.76	33.92	34.58
A (Å)	5.135	5.08	5.117
B (Å)	5.184	5.19	5.175
C (Å)	5.302	5.22	5.291
B (deg)	99.48	99.77	99.22

[a]Reference 27.
[b]Reference 28.

To simulate the surface we employ slab geometry and symmetric slabs. In the direction normal to the surface, a 15-Å-thick vacuum layer is added to eliminate spurious slab-slab interactions. We use the conjugate-gradient algorithm to optimize the atomic structure for various surface terminations of hafnia polymorphs. The surface energy of a vacuum-cleaved surface is then estimated using the zero-temperature "grand canonical" thermodynamic potential,[30]

$$E_s = \frac{1}{2A}\{E_{\text{slab}} - N_{O_2}\mu_{O_2} - N_{O_2}E_{O_2} - N_{\text{Hf}}\mu_{\text{Hf}} - N_{\text{Hf}}E_{\text{Hf}}\}. \quad (1)$$

Here the energy is given per surface unit cell, and the factor of 1/2 is due to having two interfaces in the supercell. The chemical potentials of Hf and O_2 are related by the equilibrium condition $\mu_{\text{Hf}}+\mu_{O_2}=-E_{HfO_2}$. Here E_{HfO_2} is the formation energy of hafnia; the chemical potential of HfO_2 is set to zero since we are in equilibrium with the bulk. Therefore the surface-free energy is a function of one chemical potential only. We choose the chemical potential of oxygen, and it is set to change in the energy window from zero (equilibrium with oxygen supply) to negative energy of formation of hafnia E_{HfO_2} (below this value Hf metal will start forming on

the surface). For hydrogen-passivated surfaces Eq. (1) needs to be modified,[31]

$$E_s = \frac{1}{2A}\{E_{\text{slab}} - N_{O_2}\mu_{O_2} - N_{O_2}E_{O_2} - N_{\text{Hf}}\mu_{\text{Hf}} - N_{\text{Hf}}E_{\text{Hf}} - N_{H_2}E_{H_2} - N_{H_2}\mu_{H_2}\}. \quad (2)$$

Note that the chemical potential of hydrogen is given with respect to H_2 molecule and can be written as function of pressure and temperature as follows:

$$\mu_{H_2} = kT\left[\ln\left(\frac{pV_Q}{kT}\right) - \ln Z_{\text{rot}} - \ln Z_{\text{vib}}\right],$$

where p is the hydrogen partial pressure, T is temperature, and Z_{rot} and Z_{vib} are the rotational and vibrational partition functions, respectively. We now discuss several surfaces of monoclinic and tetragonal phases in more details with the emphasis on the former since the dominant phase in the ALD-grown hafnia thin films is monoclinic.

A. Monoclinic

Because of low symmetry of the monoclinic phase, cutting a surface from a monoclinic crystal theoretically is not a trivial task. The slabs thus generated are not unique. We construct several structures with different orientations and stoichiometries. Then we relax them using VASP and use the total energies of optimized structures to calculate the surface energy of each termination as a function of chemical potential according to Eq. (1). In Fig. 5(a) we plot the surface energy for different orientations for the monoclinic phase as a function of the oxygen chemical potential, the zero value of which indicates equilibrium with the oxygen supply and thus describes the oxygen-rich environment. As seen in Fig. 5(a) all stoichiometric surfaces have surface energies independent of the chemical potential. For the stoichiometric surfaces our calculations agree well with those presented in Refs. 12 and 13. We compare our results to those in Ref. 12 in Table II. The order and values of surface energy for the relaxed stoichiometric surfaces are in good agreement. In addition, we consider several nonstoichiometric and H-passivated surfaces as shown in Fig. 5(a). Two surfaces with the lowest surface energy among the non-H-passivated surfaces are the stoichiometric $(11\bar{1})$ and oxygen-rich $(11\bar{2})$. Under extreme oxygen-rich conditions the oxygen-terminated (001) surface becomes comparable to $(11\bar{1})$ in energy. The stoichiometric $(11\bar{1})$ surface has the lowest surface energy in most of the allowed range of the chemical potential (with the exception of the extreme oxygen-rich regime). This might explain why thin hafnia films in our experiments (as well as in reports by others[9]) favor the texture axis normal to $(11\bar{1})$ planes. However, under certain conditions,[11] hafnia films may favor (001) as the growth direction. Taking into account that the $HfCl_4$ precursor requires water cycle during the film deposition, the effect of surface hydroxylation needs to be considered. In general, the amount of hydrogen on the surface of a growing film depends on the density of undercoordinated oxygen atoms, and on the details of purging and temperature, and thus

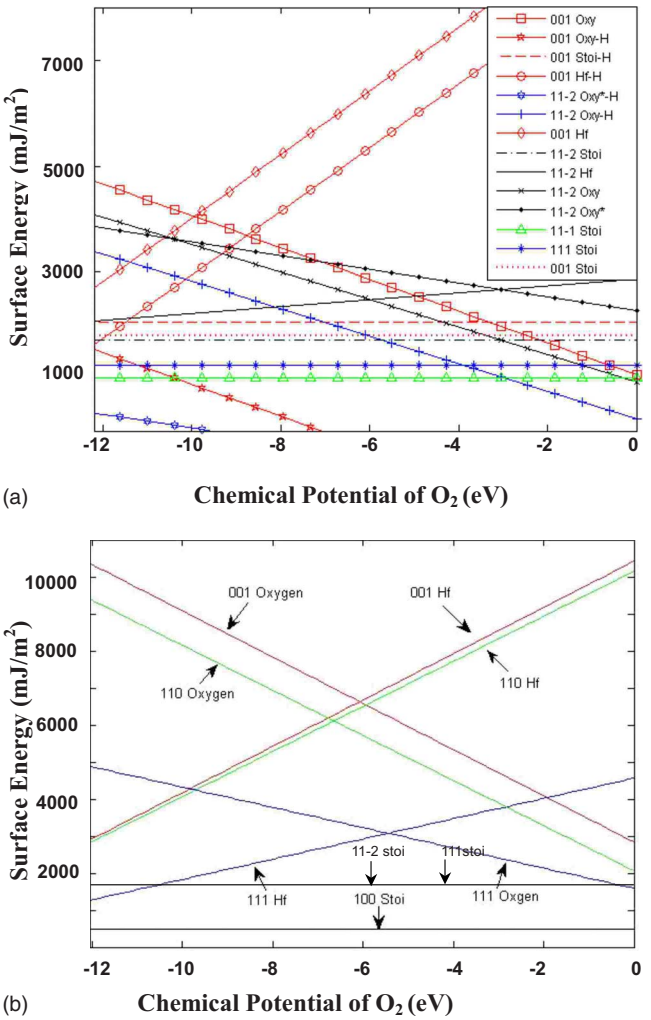

FIG. 5. (Color online) (a) Surface energy of several surfaces of monoclinic HfO_2 as a function of the oxygen chemical potential. Labels ending in "Oxy," "Hf," and "Stoi" refer to oxygen, hafnia, and stoichiometric terminations, respectively. Labels ending in "H" refer to hydrogen passivation. In the case of two oxygen-terminated $(11\bar{2})$ surfaces, the termination with less oxygen is marked with an asterisk. (b) Surface energy of several surfaces of tetragonal HfO_2 with different termination and orientation. Labels indicate the orientation and termination of a particular surface.

is specific to the growth process. We calculate the surface energy of hydrogen-passivated surfaces using Eq. (2). A comprehensive account of this study will be presented elsewhere. For the present argument it is sufficient to note that the presence of hydrogen on stoichiometric and Hf-terminated surfaces does not change the surface energy and geometry drastically. However, the hydroxylation has a rather big impact on O-terminated surfaces, such as the oxygen-terminated (001) surface. As seen in Fig. 5(a) the surface energy of hydroxylated (001) oxygen-terminated surface is reduced by 3200 mJ/m^2 relative to the original surface. A similar effect has been previously reported by us for the crystalline SiO_2 surfaces.[31] This might explain the stabilization of (001) surface for monoclinic hafnia reported by other workers. Also, oxygen-terminated $(11\bar{2})$ surfaces are

TABLE II. Surface energy of monoclinic hafnia with stoichiometric termination.

Stoichiometric surface	Surface energy in (J/m^2) from Ref. 12		Surface energy in (J/m^2) from this work
	Unrelaxed	Relaxed	
$(\bar{1}11)$	1.46	0.993	1.04
(111)	1.562	1.199	1.25
(001)	2.169	1.416	1.45
$(11\bar{2})$			1.71
(100)	2.165	1.667	1.79

stabilized under either oxygen-poor or oxygen-rich conditions. We now shall focus on the most stable hydrogen-free surfaces of the monoclinic phase and compare their atomic and electronic structures.

As we have discussed in Sec. III A, for the 40 Å hafnia film the $(11\bar{2})$ direction is consistent with the texture axes normal to the film surface. According to our thermodynamic analysis this termination is stable under oxygen-rich conditions. Therefore we consider one stoichiometric and one oxygen-terminated surface with the $(11\bar{2})$ orientation [shown in Figs. 6(a) and 6(b), respectively]. The stoichiometric model referred to as slab I [Fig. 6(a)] contains 32 oxygen and 16 hafnia atoms and is 9.6 Å thick. The oxygen-terminated model referred to as slab II [Fig. 6(b)] contains 40 oxygen and 16 hafnia atoms and is 11.2 Å thick. The top and bottom surface atomic configurations of the slab are essentially the same, albeit rotated with respect to one another, in both cases. The lateral lattice constants of slabs I and II are listed in Table III. The structures of slabs I and II shown in Figs. 6(a) and 6(b) are fully relaxed. The most obvious difference between the two is that the latter structure has several peroxy bonds between pairs of oxygen atoms on the surface and the former has no such bonds. Peroxy bonds are known in metal oxides[31] but have not been reported for hafnia; they appear in this structure because there are not enough hafnium atoms to be bonded to oxygen on the surface; this is the energy lowering mechanism of the oxygen-rich surface. The presence of peroxy bonds affects the electronic structure of the surface, as we shall discuss in detail below.

The theoretical GGA band gap of HfO_2 is only 4.1 eV [the local-density approximation (LDA) gap is 3.8 eV and experimentally it is 5.8 eV]. The top of the valence band is comprised predominantly of the oxygen *p* state and the bottom of the conduction band is mainly hafnium *d* states.[27] In Fig. 7(a) we show the total density of states for the slab with the oxygen-rich $(11\bar{2})$ surface discussed above. The Fermi level is pinned by a state 3.8 eV above the valence-band top. The level is a filled state of the peroxy bond. In Fig. 7(b) we show partial density of states (PDOS) projected onto several oxygen atoms labeled in Fig. 6(b). Atoms 3 and 4 of the second peroxy bond contribute to this peak. The state 2.7 eV below the Fermi level corresponds to the first peroxy bond. We can also see the "proper" surface states (atom 5) 0.2 eV above the valence-band top. The valence-band top is 3.8 eV

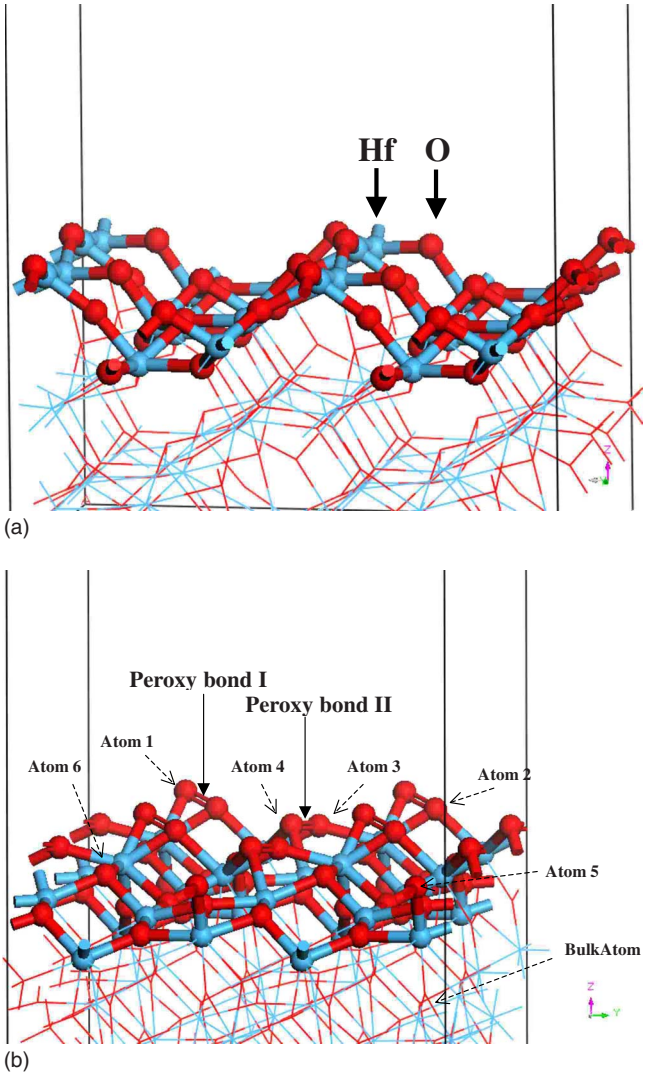

FIG. 6. (Color online) (a) The relaxed structure of the stoichiometric $(11\bar{2})$ slab of monoclinic hafnia with 32 oxygen atoms and 16 hafnia atoms. (b) The relaxed structure of the oxygen-rich oxygen-terminated $(11\bar{2})$ monoclinic slab with 36 oxygen atoms and 16 hafnia atoms.

below the Fermi level as can be seen from the lowest panel in Fig. 7(b). It is useful to project the PDOS onto oxygen atoms across the slab and plot the $l=1$ component (*p* state) layer by layer as in Fig. 7(c). We can see that the surface states coming from the peroxy bonds are rapidly decaying as we move deeper into the slab. Yet the proper surface state right at the band edge decays with a slower rate. Clearly the behavior of these surface states is quite different and can be understood with the complex band structure. The complex band structure of the monoclinic phase suggests that the de-

TABLE III. The simulation cell parameters used to calculate the slab of the $(11\bar{2})$ surface of monoclinic hafnia.

a	*b*	α	β	γ
8.49 Å	7.30 Å	90°	90°	94.78°

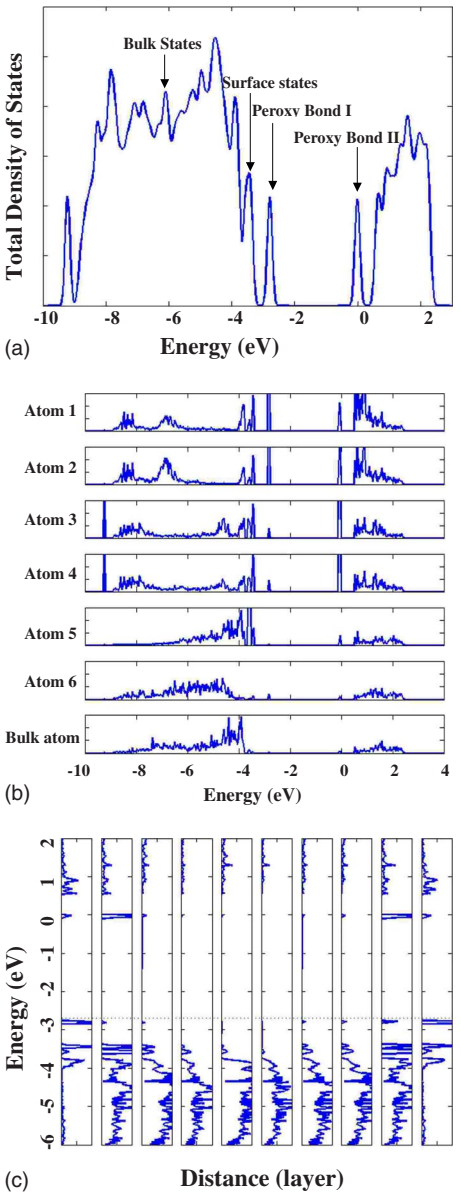

FIG. 7. (Color online) (a) The total density of states of $(11\bar{2})$ oxygen-rich monoclinic hafnia plotted in the energy window from −12.0 to 4.0 eV. (b) The partial density of states projected on the oxygen atoms labeled in Fig. 6(b). (c) The oxygen-projected density of states plotted layer by layer along the z axis of the oxygen-terminated slab.

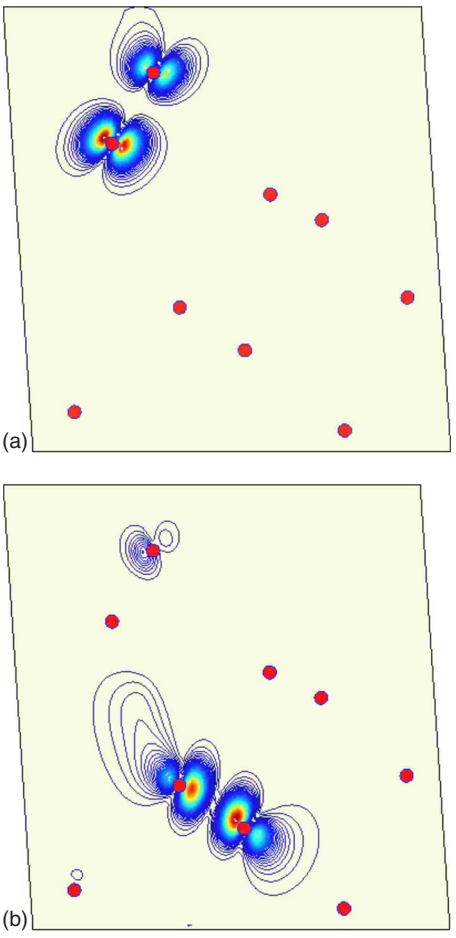

FIG. 8. (Color online) (a) The partial electron-density distribution coming from the localized states 2.7 eV below the Fermi level for the oxygen-rich $(11\bar{2})$ monoclinic surface [see Fig. 6(b)]. Dots represent oxygen atoms at the surface. (b) The partial electron-density distribution coming from the states right at the Fermi level of the oxygen-rich $(11\bar{2})$ monoclinic surface.

cay length of both evanescent states corresponding to the peroxy bonds should be about 2 Å, while the gap states close to the band edge decay much slower.[32] Figure 8 shows the electron-density distribution corresponding to the peroxy states. In Fig. 8(a) we show the contour plot (in the surface plane) of the electron density corresponding to the lower-energy peroxy state. It looks like an antibonding $pp\pi$ orbital of the peroxy dimer. In Fig. 8(b) we show the contour plot in the subsurface plane of the electron density corresponding to the surface state at the Fermi level. It is clearly an antibonding $pp\sigma$ orbital of the other peroxy bond II. Note that the valence-band top does not show any bending across the film. This is because the peroxy state pins the Fermi level approximately midgap. Peroxy bonds on oxide surfaces are well documented.[33–35] They play important role in surface catalysis. However we are unaware of studies focused specifically on hafnia. Currently we are investigating surface vibrational properties of hafnia; the results may be used to identify peroxy bonds by Raman spectroscopy. We hope our work will inspire further experimental effort.

B. Tetragonal

When compared with the monoclinic phase, the structure of tetragonal hafnia has higher symmetry. Thus the number of possible surface terminations of the tetragonal phase is limited. Most surfaces of tetragonal hafnia are either oxygen terminated or hafnia terminated, with the exception of the (100) surface that can only be cut stoichiometric.

In Fig. 5(b) we plot the surface energy for different orientations of the tetragonal phase as a function of the oxygen chemical potential. The plots with a positive slope correspond to hafnium-terminated surfaces and those with a negative slope correspond to oxygen-terminated surfaces. The

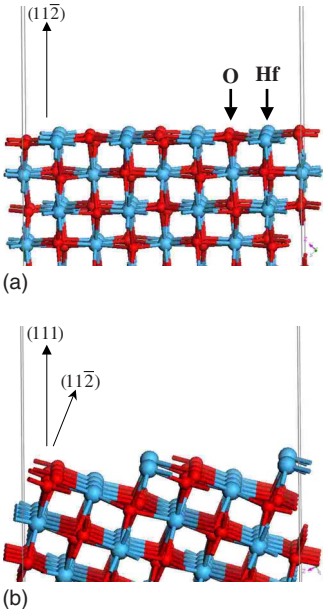

FIG. 9. (Color online) (a) The relaxed (11$\bar{2}$) structure of the tetragonal hafnia stoichiometric slab with 32 oxygen atoms and 16 hafnia atoms. (b) The relaxed (111) structure of the tetragonal stoichiometric hafnia slab with 32 oxygen atoms and 16 hafnia atoms.

surface energy of stoichiometric surfaces does not depend on the chemical potential. Among the nonstoichiometric surfaces the (111) family has lowest surface energy. However, the stoichiometric (100) surface is the most stable termination of tetragonal hafnia. This is in contrast to tetragonal zirconia where the most stable surface is (111).[36] We should note that the surface described as (111) in Ref. 36 is actually stoichiometric (11$\bar{2}$). The real (111) surface of both *t* hafnia and *t* zirconia is built of (11$\bar{2}$) facets [see Figs. 9(a) and 9(b)]. We have considered both oxygen and hafnium terminated (111) as well as a stoichiometric termination. Surprisingly, in terms of surface energy the stoichiometric (11$\bar{2}$) and (111) terminations are indistinguishable [see Fig. 5(b)].

In Fig. 10 we analyze the average potential plot for the slab with the (111) surface for the oxygen and hafnium terminations. Figure 10(a) shows a combined plot of the plane-averaged electrostatic potential and its macroscopic average for hafnia-terminated (111) surface across the thickness of the slab along with the plane by plane projected oxygen density of states. Oxygen is chosen since the top of the valence band in hafnia is predominantly the oxygen *p* state. The Fermi level is pinned by the midgap surface state. The state is mostly a dangling hafnia *d* orbital but is obviously hybridized with the oxygen *p* orbital. The surface state results in a double layer that lowers the bulk potential by about 0.2 eV. The work function can be estimated as a difference between the Fermi level and the value of the potential in the vacuum region. We also estimate the electron affinity, but for that we use the bulk value of the reference potential. In the bulk the valence-band top is 2.4 eV higher than the average electrostatic potential. Using the experimental value of the HfO_2 band gap of 5.7 eV, we estimate the electron affinity to be 1.95 eV. If we now apply a *GW* correction of 0.57 eV [calculated for the top of the valence band at the Γ point of bulk *m*-HfO_2 (Ref. 37)], we arrive at the value of 2.52 eV similar to that measured in recent experiments.[38] Figure 10(b) shows similar data for the oxygen-terminated (111) *t*-HfO_2 surface. Here the highest-occupied surface state is located 0.4 eV above the top of the valence band and is oxygen related. The results for the work function and electron affinity of different terminations of tetragonal and monoclinic phases are summarized in Table IV.

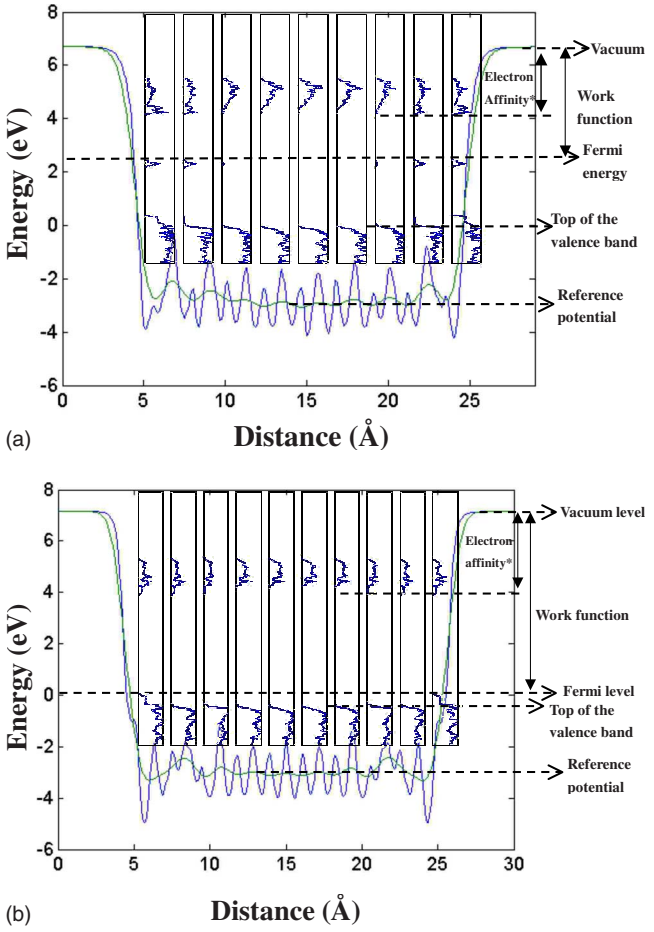

FIG. 10. (Color online) (a) A composite graph of the plane-averaged electrostatic potential used as the energy reference, its macroscopic average, and the plane by plane projected oxygen density of states for the Hf-terminated (111) surface of *t*-HfO_2. The surface state which is actually a dangling Hf *d* orbital is clearly seen pinning the Fermi level. (b) Same as (a) for the O-terminated (111) surface of *t*-HfO_2

C. Role of surface energy in the *m*-*t* transformation

The phase composition of a thin film is important in view of the uniformity requirements since the electrical properties may change significantly between different polymorphs.[5,31] In the case of very thin films the difference in the surface energy of different polymorphs may stabilize higher-energy phases. Experimentally, in zirconia the stabilization of tetragonal grains below the critical size of R_c=150 Å has been reported[39] and discussed from the theory point of view by

TABLE IV. The work function and electron affinity of various hafnia surfaces. To estimate the electron affinity the 5.7 eV value is used for the bulk band gap for both phases. The *GW* correction is applied to the valence-band edge (see text).

	Tetragonal					Monoclinic	
	$(11\bar{2})_{stoi}$ (eV)	$(111)_{stoi}$ (eV)	$(111)_{Hf}$ (eV)	$(111)_{oxy}$ (eV)	$(100)_{stoi}$ (eV)	$(11\bar{1})_{stoi}$ (eV)	$(11\bar{2})_{oxy}$ (eV)
Work function	6.78	6.83	4.82	7.65	6.71	7.30	7.29
Electron affinity	1.08	1.13	1.99	2.52	1.71	1.82	1.59

Christensen and Carter.[36] In hafnia a similar effect has been also observed.[7] As we have shown the lowest surface energy for tetragonal hafnia is achieved for the (001) orientation. This is 500 mJ/m^2 lower than the most stable $(11\bar{1})$ stoichiometric termination of monoclinic hafnia; the difference is much larger than that reported for zirconia.[36] Thus in a very thin film one may hope to suppress the tetragonal to monoclinic transition. Ignoring the small difference in molar volumes of tetragonal and monoclinic hafnia and the entropic effects, the critical size can be roughly estimated as follows. In a uniform hafnia film of thickness R and area A, the phase equilibrium equation defines the critical thickness,

$$A\gamma_t + AR_cE_t = A\gamma_m + AR_cE_m,$$

where γ_t and γ_m are the lowest surface energies for the tetragonal and monoclinic phases, respectively. E_t and E_m are the bulk energy densities for the two phases, and R_c is the critical thickness. Thus the critical thickness R_c is given by

$$R_c = \frac{\gamma_m - \gamma_t}{E_t - E_m}.$$

Using our calculated bulk energies and surface energies calculated for the stoichiometric $(11\bar{1})$ surface of monoclinic hafnia and (100) stoichiometric surface of tetragonal hafnia, we estimate that for films thinner than 15 Å the presence of tetragonal phase may be expected. If a spherical grain is considered the critical radius is 45 Å. Experimentally, however, we observe the presence of the tetragonal phase only in 99-Å-thick films. This might suggest the presence of small-size crystallites in these films and not in the thicker or thinner ones. Clearly, other mechanisms such as the presence of hydrogen and point defects (i.e., oxygen vacancies) could be responsible for the stabilization of a high-symmetry phase. In addition, we have not considered the energy of grain boundaries which might be more appropriate than surface energies for this case. Therefore we view our findings as consistent with the surface-energy-driven suppression of the phase transition rather than as proving it.

V. CONCLUSIONS

We analyze the properties of ultrathin hafnia films grown by ALD using hafnium tetrachloride and water at 300 °C. Films thicker than 200 Å after annealing at 900–1000 °C are determined to consist of the monoclinic phase with {1,1,1} and $\{\bar{1}11\}$ texturing. Surprisingly, films of the intermediate thicknesses (between 70 and 100 Å) are found to consist of a mixture of monoclinic and tetragonal phases (and show no texturing after a 500 °C annealing). The thinner 40 Å film after the 500 °C annealing is phase uniform, monoclinic, and textured along the $\{21\bar{1}\}$ and $\{11\bar{2}\}$ axes. The first-principles calculations of the surface phase diagram for monoclinic and tetragonal hafnia reveal that in the absence of hydrogen, (111) and $(\bar{1}11)$ are the lowest-energy surface terminations of monoclinic hafnia under a wide range of chemical environment, consistent with texturing of thick hafnia films. Due to the use of tetrachloride precursor, the ALD is performed on the oxidized surface of a Si wafer. Since the thin SiO_2 layer is amorphous, the crystallographic effect of the substrate is minimal. Therefore one could expect that either the growth kinetics or thermodynamics dominate the film growth. Our results suggest that thermodynamics plays a role (or that the lowest-energy surface is also the fastest growing one). In addition, the calculations suggest that in the presence of hydrogen the $(11\bar{2})$ termination can be stabilized both under oxygen-rich and oxygen-poor conditions, which might explain the peculiar texturing of very thin monoclinic films. The most intriguing result is the quenching of the tetragonal phase at room temperature for intermediate film thicknesses. It is possible that extremely small grains of tetragonal hafnia are stabilized owing to the lower surface energy of that phase. According to our calculations, in vacuum the critical thickness necessary to stabilize tetragonal hafnia is between 1 and 40 Å. This is consistent with the large width of the electron-diffraction peaks attributed to the tetragonal phase. The presence of multiple phases in hafnia films may have important device implications. It has been shown that electronic properties such as the dielectric constant[5] and the charge neutrality level[32] vary significantly from one polymorph to another, thus causing fluctuations of such important parameters as the threshold voltage. In addition, we have examined the work function and electron affinity for several surfaces of monoclinic and tetragonal hafnia. In the case of the tetragonal phase we find a large variation in electron affinity depending on the surface termination. For the oxygen-terminated (111) surface of the tetragonal hafnia the electron affinity is estimated to be 2.52 eV when a quasiparticle correction is included. For the monoclinic phase the electron affinity shows much less variation and is about 1.7 eV for the most stable (111) oriented stoichiometric surface, in good agreement with experiment.

ACKNOWLEDGMENTS

It is our pleasure to thank Alex Navrotsky, Sergey Usha-

kov, John G. Ekerdt, Tuo Wang, David Gilmer, and Jamie Schaefer for many insightful discussions we had in the course of this work. This work is in part supported by the National Science Foundation under Grant No. DMR-0606464 and Texas Advanced Computing Center (A.A.D. and X.L.).

*demkov@physics.utexas.edu

[1] 2007 International Technology Roadmap for Semiconductors, Semiconductor Industry Association, San Jose, 2007.
[2] G. D. Wilk, R. M. Wallace, and J. M. Anthony, J. Appl. Phys. **89**, 5243 (2001).
[3] M. Copel, M. Gribelyuk, and E. Gusev, Appl. Phys. Lett. **76**, 436 (2000).
[4] M. Gutowski, J. E. Jaffe, C. Liu, M. Stoker, R. I. Hegde, R. S. Rai, and P. J. Tobin, Appl. Phys. Lett. **80**, 1897 (2002).
[5] X. Zhao and D. Vanderbilt, Phys. Rev. B **65**, 233106 (2002).
[6] M. Ritala, M. Leskela, L. Niinisto, T. Prohaska, G. Friedbacher, and M. Grasserbauer, Thin Solid Films **250**, 72 (1994).
[7] S. V. Ushakov, A. Navrotsky, Y. Yang, S. Stemmer, K. Kukli, M. Ritala, M. A. Leskelä, P. Fejes, A. A. Demkov, C. Wang, B. Y. Nguyen, D. Triyoso, and P. Tobin, Phys. Status Solidi B **241**, 2268 (2004).
[8] Q. Fang, J.-Y. Zhang, Z. Wang, M. Modreanu, B. J. O'Sullivan, P. K. Hurley, T. L. Leedham, D. Hywel, M. A. Audier, C. Jimenez, J.-P. Senateur, and I. W. Boyd, Thin Solid Films **453-454**, 203 (2004).
[9] M. Y. Ho, H. Gong, G. D. Wilk, B. W. Busch, M. L. Green, P. M. Voyles, D. A. Muller, M. Bude, W. H. Lin, A. See, M. E. Loomans, S. K. Lahiri, and P. T. Räisänen, J. Appl. Phys. **93**, 1477 (2003).
[10] D. Triyoso, R. Liu, D. Roan, M. Ramon, N. V. Edwards, R. Gregory, D. Werho, J. Kulik, G. Tam, E. Irwin, X. D. Wang, L. B. La, C. Hobbs, R. Garcia, J. Baker, B. E. White, and P. Tobin, J. Electrochem. Soc. **151**, F220 (2004).
[11] J. Aarik, A. Aidla, H. Mändar, V. Sammelselg, and T. Uustare, J. Cryst. Growth **220**, 105 (2000).
[12] I. M. Iskandarova, A. A. Knizhnik, E. A. Rykova, A. A. Bagatur'yants, B. V. Potaptkin, and A. A. Korkin, Microelectron. Eng. **69**, 587 (2003).
[13] A. B. Mukhopadhyay, J. F. Sanz, and C. B. Musgrave, Phys. Rev. B **73**, 115330 (2006).
[14] D. H. Triyoso, R. I. Hegde, J. Grant, P. Fejes, R. Liu, D. Roan, M. Ramon, D. Werho, R. Rai, L. B. La, J. Baker, C. Garza, T. Guenther, B. E. White, Jr., and P. J. Tobin, J. Vac. Sci. Technol. B **22**, 2121 (2004).
[15] M. Ritala and M. Leskela, in *Handbook of Thin Films Materials*, edited by H. S. Nalwa (Academic, Cambridge, 2001), p. 103.
[16] M. Ritala, M. Leskela, L. Niinisto, T. Prohaska, G. Friedbacher, and M. Grasserbauer, Thin Solid Films **250**, 72 (1994).
[17] H. Kim, P. McIntrye, and K. Saraswat, Appl. Phys. Lett. **82**, 106 (2003).
[18] G. Scarel, C. Wiemer, S. Ferrari, G. Tallarida, and M. Fanciulli, Proc. Est. Acad. Sci., Phys., Math. **52**, 308 (2003).
[19] H.-H Tseng, M. E. Ramon, L. Hebert, P. J. Tobin, D. Triyoso, J. M. Grant, Z. X. Jiang, D. Roan, S. B. Samavedam, D. C. Gilmer, S. Kalpat, C. Hobbs, W. J. Taylor, O. Adetutu, and B. E. White, Tech. Dig. - Int. Electron Devices Meet. **2003**, 4.1.1.
[20] JCPDF Card No. 08-0342.
[21] JCPDF Card No. 06-0318.
[22] J. Wang, H. P. Li, and R. Stevens, J. Mater. Sci. **27**, 5397 (1992).
[23] G. Kresse and J. Furthmuller, Phys. Rev. B **54**, 11169 (1996).
[24] J. P. Perdew, Physica B **172**, 1 (1991).
[25] J. P. Perdew, Phys. Lett. A **165**, 79 (1992).
[26] D. Vanderbilt, Phys. Rev. B **41**, 7892 (1990).
[27] A. A. Demkov, Phys. Status Solidi B **226**, 57 (2001).
[28] J. Wang, H. P. Li, and R. Stevens, J. Mater. Sci. **27**, 5397 (1992).
[29] J. Adam and M. D. Rodgers, Acta Crystallogr. **12**, 951 (1959).
[30] J. Padilla and D. Vanderbilt, Surf. Sci. **418**, 64 (1998).
[31] E. Chagarov, A. A. Demkov, and J. B. Adams, Phys. Rev. B **71**, 075417 (2005).
[32] A. A. Demkov, L. R. C. Fonseca, E. Verret, J. Tomfohr, and O. F. Sankey, Phys. Rev. B **71**, 195306 (2005).
[33] R. Q. Long, Y. P. Huang, and H. L. Wan, J. Raman Spectrosc. **28**, 29 (1997).
[34] V. V. Pushkarev, V. I. Kovalchuk, and J. L. d'Itri, J. Phys. Chem. B **108**, 5341 (2004).
[35] C. Li, K. Domen, K. Maruya, and T. Onishi, J. Am. Chem. Soc. **111**, 7683 (1989).
[36] A. Christensen and E. A. Carter, Phys. Rev. B **58**, 8050 (1998).
[37] O. Sharia (private communication).
[38] E. Bersch, S. Rangan, R. A. Bartynski, E. Garfunkel, and E. Vescovo, Phys. Rev. B **78**, 085114 (2008).
[39] G. Cerrato, S. Bordiga, S. Barbera, and C. Morterra, Surf. Sci. **377-379**, 50 (1997).